Title
Local pH control for impure-water-fed bipolar-membrane electrolyzers

Journal
Energy & Environmental Science

ISSN
1754-5692

Authors
Han, Sanghwi
Choi, Gwan Hyun
Zhang, Wenbo
et al.

Publication Date
2026-08-05

DOI
10.1039/d6ee02476a

ARTICLE

Local pH control for impure-water-fed bipolar-membrane electrolyzers

Sanghwi Han[a,b], Gwan Hyun Choi[a,b], Wenbo Zhang[a,b], Dawei Xi[a,b], Duha Syar[a,b], Jaehyuk Shim[c,d], Jang Yong Lee[e], Thomas F. Jaramillo[c,d], Jaeyune Ryu*[f,g,h], Shannon W. Boettcher*[a,b]

Bipolar membrane (BPM) electrolyzers offer advantages in the electrolysis of impure-waters by controlling ion flux, yet still suffer from performance and durabilty limitations. Here, we investigate the impact of NaCl electrolyte (nominally simulated seawater) on BPM electrolyzer operation and identify local pH gradients at electrode–membrane interfaces, arising from coupled ion transport and electrode reactions, as one origin of performance loss and degradation. NaCl in the catholyte induces pronounced pH gradients at the cathode | cation-exchange-layer interface, leading to increased voltage, while partial Cl^- crossover to the anode becomes detrimental under locally OH^--deficient conditions, promoting the chlorine evolution reaction and accelerating degradation. Direct physical integration of the cathode and anode catalysts onto the cation and anion exchange layers through spray coating and electrodeposition, respectively, mitigates these effects by minimizing the membrane–catalyst distance. The BPM electrolyzer built in this way achieves 0.50 A cm^{-2} at 2.8 V and shows a degradation rate of 5.5 mV h^{-1} over 120 h in 0.50 M NaCl electrolyte, compared to degradation of 71 mV h^{-1} with a typical porous-transport-layer device structure. This work thus establishes control of local pH gradients as a design principle for BPM electrolysis with impure-water feeds.

Introduction

Bipolar membranes (BPMs) consist of a cation exchange layer (CEL) and an anion exchange layer (AEL), typically integrated with a catalytic interface layer. The fixed negative and positive charge groups in the CEL and AEL, respectively, enable BPMs to suppress co-ion crossover through the Donnan exclusion effect.[1–5] Under reverse bias operation, BPMs drive water dissociation (WD, $H_2O \rightarrow H^+ + OH^-$) at the CEL/AEL junction to carry ion current and allow the maintenance of a steady-state pH gradient between the cathode (low pH) and anode (high pH).[6–9] In seawater electrolysis with BPM systems, it is beneficial to supply the impure electrolyte exclusively as the catholyte as the CEL suppresses Cl^- crossover, while the alkaline environment maintained at the anode/AEL reduces the likelihood of the chlorine evolution reaction (ClER).[10] Consequently, BPM electrolyzers offer advantages for impure-water operation compared to conventional monopolar membrane systems.[11–14]

Despite these attributes, BPM electrolyzers remain vulnerable to operation in impure electrolytes. In an asymmetric configuration employing 0.50 M NaCl as the catholyte and pure-water as the anolyte, the NaCl-containing catholyte induced a large voltage penalty of ~0.9 V at 500 mA cm^{-2} compared to a pure-water electrolyte.[15] In addition, some co-ion crossover persists in BPM-based systems.[16,17] Under weakly buffered asymmetric conditions, ion migration, diffusion, water dissociation, and the hydrogen evolution reaction/oxygen evolution reaction (HER/OER) can together generate strong local chemical and pH gradients at membrane–electrode interfaces. Minority Cl^- crossover, together with limited local OH^- availability at the anode, is associated with slow acidification (reaching pH ≈ 3 within 2 h at 250 mA cm^{-2}),[18] under which the ClER becomes increasingly facile over the OER.[19–21] The ClER products are expected to accelerate the degradation of the membranes and catalysts.[22] These observations underscore the need to elucidate how impure electrolytes influence BPM electrolyzers and to develop strategies to mitigate losses from these ionic processes. However, the roles of individual ionic species in governing interfacial reactions, crossover, and long-term stability remain insufficiently understood, particularly in terms of how they couple to local pH at membrane–electrode interfaces, hindering the design of BPM electrolyzers for salt-water and other feeds with multiple ionic species.

Here, we study the impact of 0.50 M NaCl electrolyte on BPM electrolyzer operation and identify local pH gradients at electrode–membrane interfaces, arising from coupled ion transport

[a]*Department of Chemical and Biomolecular Engineering and Department of Chemistry, University of California, Berkeley, California 94720, United States*
[b]*Energy Technology and Systems Division, Lawrence Berkeley National Laboratory, Berkeley, California 94720, United States*
[c]*Department of Chemical Engineering, Stanford University, Stanford, California 94305, United States*
[d]*SUNCAT Center for Interface Science and Catalysis, SLAC National Accelerator Laboratory, Menlo Park, California 94025, United States*
[e]*Department of Chemical Engineering, Konkuk University, Seoul 05029, Republic of Korea*
[f]*Department of Chemical and Biological Engineering, Institute of Chemical Processes, Seoul National University, Seoul 08826, Republic of Korea*
[g]*Center for Nanocrystal Research, Institute for Basic Science (IBS), Seoul 08826, Republic of Korea*
[h]*SNU Energy Initiative, Seoul National University (SNU), Seoul 08826, Republic of Korea*
Supplementary Information available: [details of any supplementary information available should be included here]. See DOI: 10.1039/x0xx00000x

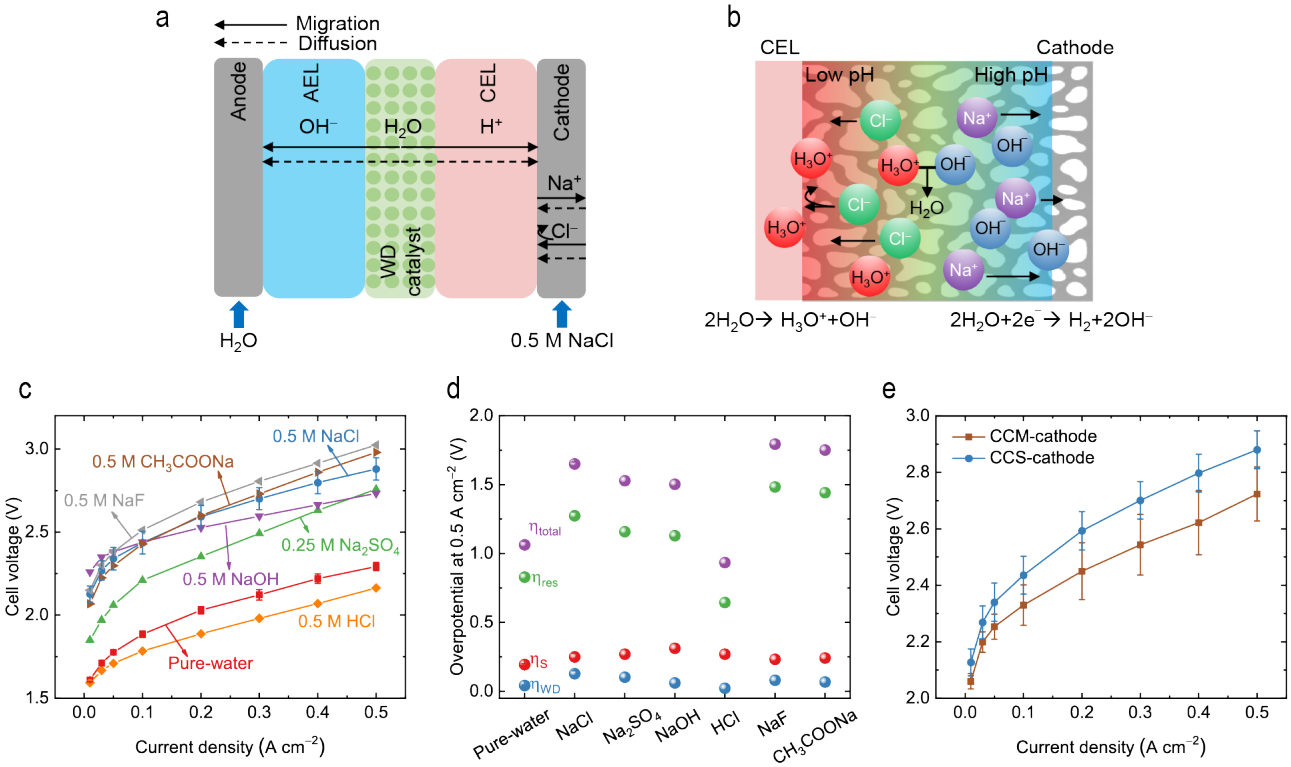

Fig. 1. Electrochemical behaviour of BPM electrolyzers as a function of catholyte composition. (a) Schematic of ion transport under reverse-bias conditions in a NaCl-fed BPMWE system. Solid lines indicate ion migration driven by the electric field, while dashed lines represent the direction of diffusion-driven flux. (b) Schematic of ion transport and the local pH gradient at the porous cathode/CEL interface. The pH gradient is represented by a colour scale, ranging from red (lower pH) to blue (higher pH). (c) Polarization curves of the BPM electrolyzer operated at 60 °C with pure water at the anode and various electrolytes at the cathode. (d) Overpotential distributions at a current density of 0.50 A cm^{-2}. (e) Comparison of polarization curves in BPM electrolyzers operated with a pure-water anolyte and 0.50 M NaCl catholyte using cathodes fabricated as a catalyst-coated membrane (CCM) and a catalyst-coated substrate (CCS).

and electrode reactions, as a source of performance loss and degradation. The NaCl in the catholyte induces pH gradients at the cathode–CEL interface, leading to increased voltage from concentration polarization, while partial Cl^- crossover to the anode becomes especially detrimental under locally OH^--deficient conditions, promoting the ClER and accelerating durability failure. By integrating the cathode and anode catalysts onto the CEL and AEL directly via spray coating and electrodeposition, respectively, the local pH gradients through the catalyst layers are reduced, resulting in improved performance and durability. We also quantified, and analysed via a semi-quantitative model, the net water transport in both the anolyte and catholyte of the BPM electrolyzer, analysing changes in water mass arising from evaporation, osmosis, electro-osmosis, and water consumption during electrolysis. By adjusting the NaOH concentration in the anolyte or adding pressure to the catholyte feed, we minimized anolyte water loss associated with (electro-)osmotic transport during steady-state operation conditions.

Results and discussion

Ion-driven pH-gradient-induced voltage losses

We studied an asymmetric BPM electrolyzer with 0.50 M NaCl as a catholyte and pure-water as an anolyte (**Figs. 1a** and **S1**). This configuration was selected to isolate transport processes relevant to saline operation while avoiding the additional chemical complexity of multicomponent seawater. A $CoOOH/Co(OH)_2$-based catalyst electrodeposited on a Pt–Ti porous transport layer (PTL) was used as an anode, paired with a spray-coated Pt cathode catalyst. The high-molecular-weight hexyltrimethylammonium-tethered polycarbazole (HQPC–TMA),[23] Nafion 212, and SnO_2-based catalyst[24] were used for AEL, CEL, and WD catalyst, respectively. The optimal cathode composition was found to consist of a Pt loading of 2.0 mg cm^{-2} and an ionomer content of 20 wt% (**Fig. S2**). All electrochemical measurements were conducted at 60 °C.

Under open-circuit conditions, Na^+ and Cl^- are expected to coexist near the porous cathode catalyst layer and the CEL interface, experiencing a diffusion-driven flux toward the anode arising from the concentration gradient. Upon application of a reverse bias, Na^+ migrates toward the cathode, whereas Cl^- migrates toward the CEL, but its transport across the CEL is suppressed due to Donnan exclusion (**Fig. 1b**).[25] At the BPM interface, H^+ and OH^- generated via WD transport toward the cathode and anode, respectively (driven by a gradient in the electrochemical potential of each species caused by concentration and electric potential differences). Consequently, the H^+ generated via WD accumulates near the CEL side with Cl^-, while the OH^- produced via the HER accumulates near the cathode with Na^+. At steady state, all the current in the cell must be carried by species like OH^- and H^+ that are involved in the electrode Faradaic reactions. Salt cations, like Na^+, that cannot react, accumulate at the cathode along with OH^- generated by the HER. This spatial separation of ionic species establishes a local pH gradient across the membrane–electrolyte interface. This pH gradient shifts the cathode

HER potential on the reversible hydrogen electrode (RHE) scale, dissipating free energy as a Nernstian concentration overpotential and thereby introducing voltage losses.[26] Although the BPM electrolyzer was assembled in a zero-gap configuration, finite electrolyte-filled regions remain within the porous catalyst structure at the micro-/nanoscale, allowing concentration polarization and local pH gradients to develop between the membrane and catalyst.

To understand the impact of this pH-gradient effect, we investigated the electrochemical behavior of BPM-based electrolyzers using different catholyte compositions. Operation with a 0.50 M NaCl catholyte required a cell voltage of 2.88 V to reach 500 mA cm^{-2}, whereas the pure-water catholyte required 2.29 V at the same current density (**Fig. 1c**). Electrochemical impedance spectroscopy (EIS) analysis indicated that, relative to the pure-water system, the NaCl-based system exhibited increases of approximately 56 mV in (high-frequency) series resistance overpotential (η_s) and 86 mV in apparent WD overpotential (η_{wd}) at 500 mA cm^{-2} (**Figs. 1d** and **S2**). However, the dominant contribution to the overall voltage difference originated from the residual overpotential (η_{res}), defined as the total overpotential remaining after subtracting the ohmic and water-dissociation overpotentials, which was higher by 446 mV in the NaCl system. Notably, a comparable voltage gap of ~0.5 V was observed even at a low current density of 10 mA cm^{-2}, consistent with a substantial contribution from steady-state mass-transport-induced pH polarization.

To assess whether enhanced electrolyte flow could partially mitigate concentration gradients near the membrane–electrode interface, we varied the catholyte flow rate from 5 to 30, 50, and 100 mL min^{-1} (**Fig. S4**). However, increasing the flow rate beyond 30 mL min^{-1} resulted in only modest improvements, and the NaCl-fed system still exhibits substantially higher cell voltages than the pure-water system. These results suggest that enhanced mixing can partially alleviate concentration polarization but does not eliminate the local pH-gradient-induced voltage losses associated with the NaCl concentration polarization. All other experiments in this study were conducted at catholyte and anolyte flow rates of 30 mL min^{-1}.

To decouple the respective contributions of Na^+ and Cl^- to concentration-polarization losses, we replaced NaCl with either 0.50 M HCl or 0.50 M NaOH. Relative to the pure-water system, the HCl catholyte lowered the overpotential at 500 mA cm^{-2} by ~130 mV, whereas the NaOH catholyte increased it by ~440 mV. The HCl and NaOH systems exhibited only minor differences (<50 mV) in η_s and η_{wd}, whereas their η_{res} values differed by ~490 mV (**Fig. 1d**). In HCl electrolytes, hydronium directly supports acidic HER ($2H^+ + 2e^- \rightarrow H_2$) and minimizes local pH polarization near the cathode along with providing a high transference number for H^+. In NaOH electrolytes, HER generates OH^- ($2H_2O + 2e^- \rightarrow H_2 + 2OH^-$) while H^+ generated by WD in the BPM is neutralized near the CEL, sustaining a nonuniform acid–base environment and concomitant concentration polarization loss.[27]

The effect of the pH gradient is also evident by comparing the polarization behavior of BPM electrolysis in NaCl and NaOH electrolytes (**Fig. 1d**), which we interpret as follows. At current densities below 100 mA cm^{-2}, the cell operated in NaCl electrolyte exhibits a lower voltage than that in NaOH. This difference arises because the NaOH system maintains a large pH difference between the catholyte bulk and the CEL, which induces additional voltage loss even at low current densities. In contrast, the pH gradient in the NaCl electrolyte remains smaller in this regime, resulting in a lower cell voltage.

At higher current densities, however, the trend reverses. In the NaCl electrolyte, the separation of Na^+ and Cl^- becomes pronounced, which amplifies the pH gradient and leads to a rapid increase in cell voltage. The limited concentrations of H^+ and OH^- at the catholyte–CEL interface contribute to high ionic transport resistance. By contrast, in the NaOH system, protons generated via WD are rapidly neutralized by the abundant OH^- at the CEL interface. Because OH^-, the dominant charge carrier, is present at high concentration, ionic transport resistance remains low, enabling superior performance at high current densities.

Additional support for the existence of cathode-side pH gradients was obtained from catalyst-ionomer-dependent HER measurements (**Fig. S5**). Pt cathodes prepared with Nafion ionomer exhibited the highest activity under pure-water operation, consistent with efficient proton transport within the catalyst layer. However, when NaOH or NaCl was used as the catholyte, a ~0.5 V voltage penalty at 0.50 A cm^{-2} was observed. As discussed above, the introduction of supporting electrolytes leads to local alkalization near the cathode due to concentration polarization, thereby increasing the HER overpotential. When anion-exchange ionomers (HQPC-TMA or PiperION) were used at the cathode, the voltage in pure-water was larger than when Nafion was used, but the voltage increase when adding NaOH or NaCl was much lower, ~0.1–0.3 V. Under steady-state operation, these anion-conducting ionomers primarily transport HER-generated OH^-, regardless of the presence of supporting electrolyte, resulting in an intrinsically alkaline catalyst-layer environment. The smaller electrolyte-dependent voltage change observed with anion-exchange ionomers thus provides independent evidence for cathode-side alkalization and pH-gradient formation with NaCl electrolyte.

A similar trend with current density is observed regardless of the anion species, as evidenced by data for 0.50 M NaF and 0.50 M CH_3COONa electrolytes. At 0.50 A cm^{-2}, however, the NaF and CH_3COONa systems exhibit ~100 mV higher overpotentials than NaCl. This additional loss may arise from protonation of F^- and CH_3COO^- at the surface of CEL by WD-generated H^+ to form weak acids, which will form a low conductivity, mildly acidic region that may reduce the effective H^+ transport rate near the CEL.[28] The 0.25 M Na_2SO_4 system shows higher performance than NaCl across the 0–500 mA cm^{-2} range. This enhancement might be attributed to the stronger electrostatic interaction between SO_4^{2-} and Na^+, which facilitates ion-pair formation and partially suppresses the development of the pH gradient.

One strategy to mitigate the pH polarization loss is to shorten ion-transport pathways within the catalyst layer. Motivated by this concept, we fabricated Pt cathodes using both catalyst-coated substrate (CCS) and catalyst-coated membrane (CCM) configurations in BPM electrolyzers and evaluated their performance under NaCl catholyte conditions. The CCM and CCS cathodes were prepared with the same Pt loading (2.0 mg cm^{-2}), ionomer content, and spray-coating procedure. Cross-sectional scanning electron microscopy (SEM) analysis showed comparable catalyst-layer thicknesses of approximately 2-3 μm for both electrodes (**Fig. S6**). At 0.50 A cm^{-2}, the CCM configuration achieved an overpotential reduction of ~160 mV relative to the CCS configuration (**Fig. 1e**). Consistently, in a proton-exchange-membrane (PEM) electrolyzer, the CCM configuration exhibited an overpotential decrease of approximately 100 mV at 0.50 A cm^{-2} compared to the CCS system (**Fig. S7**). This comparison suggests that the larger gain in the use of the CCM configuration comes from suppression of cathode-side pH/concentration gradients under NaCl-fed BPM operation. While

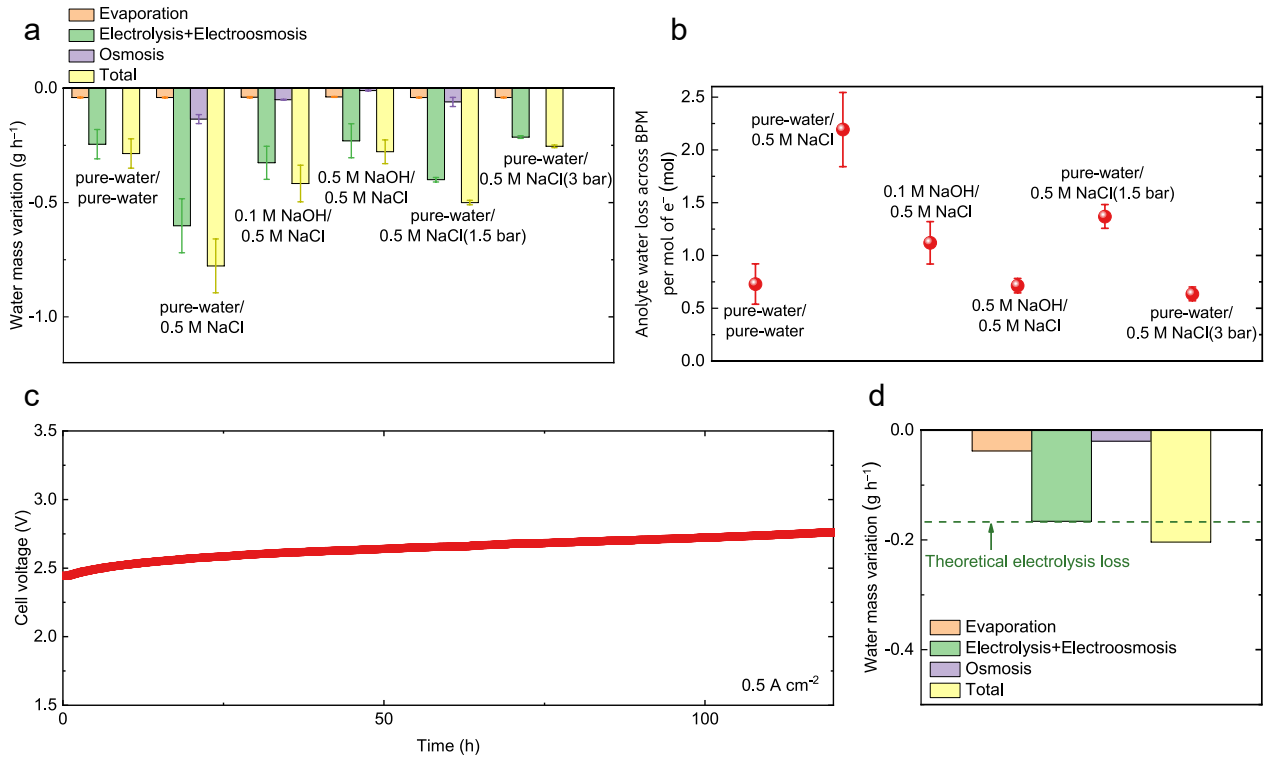

Fig. 2. Water loss in asymmetric BPM electrolyzers. (a) Time-dependent anolyte water mass variation as a function of anolyte and catholyte composition. In the notation describing each bar, the electrolytes are denoted as anolyte/catholyte. (b) Water loss per electron as a function of anolyte and catholyte composition. (c) Durability test conducted for 120 h at 0.50 A cm^{-2} and (d) cumulative anolyte water mass change over time in a BPM electrolyzer using 0.10 L of 0.50 M NaOH anolyte and 1.0 L of 0.50 M NaCl catholyte.

CCM-based PEM electrolyzers exhibit higher initial performance compared to BPM electrolyzers under NaCl operation, durability testing revealed severe ClER-induced degradation, leading to electrical shorting within 40 h (**Fig. S8**). A detailed discussion of durability and degradation is presented in a later section.

Understanding water loss from the anolyte

To assess the viability of the asymmetric BPM electrolyzer, we quantified water mass loss from the anolyte. Because water redistribution can alter local solute concentrations and interfacial pH environments during operation, it is also important for understanding the evolution of chemical gradients in the cell. In a configuration where both the anolyte and catholyte consisted of pure-water, operation at 500 mA cm^{-2} resulted in a water loss of 0.041 ± 0.002 g h^{-1} due to evaporation (due to imperfect cell and water circulation design in the test cell), while 0.24 ± 0.06 g h^{-1} was consumed by electrolysis and electro-osmotic transport (**Fig. 2a**). In contrast, the catholyte volume increased by 0.04 ± 0.02 g h^{-1} during operation (**Fig. S9**). Although it is challenging to decouple water consumption arising from electrolysis and electro-osmosis, these results indicate that in a pure-water BPM electrolyzer, water depletion occurs predominantly in the anolyte. This behavior likely arises from the higher hydration number of protons compared to hydroxide ions.[29] As H^+ ions migrate across the BPM, they transport a larger number of water molecules via electro-osmotic drag, leading to net water transfer from the anolyte to the catholyte.

When a 0.50 M NaCl catholyte was used, the anolyte water consumption increased to 0.78 ± 0.12 g h^{-1} (**Fig. 2a**). Of this amount, 0.14 ± 0.02 g h^{-1} is attributed to osmotic-driven water transport, while 0.60 ± 0.12 g h^{-1} was consumed by electrolysis and electro-osmotic transport. Under a 0.50 M NaCl catholyte, the water loss can be progressively reduced by increasing the NaOH concentration in the initial pure-water anolyte. At 0.50 M NaOH, the combined water consumption due to electrolysis and electro-osmosis decreased to 0.23 ± 0.07 g h^{-1}, which can be translated to 0.71 ± 0.07 mol_{water} per mol_{e^-}(**Fig. 2b**).

Applying pressure to the catholyte stream also reduced water loss from the anolyte. In a BPM electrolyzer with 0.50 M NaCl catholyte and pure-water anolyte, a needle valve was installed at the cathode outlet to impose a pressure difference between the catholyte and anolyte. By adjusting the valve opening, pressure differences of 1.5 and 3 bar were applied to the catholyte flow. At 1.5 bar, the osmotic water loss was 0.06 ± 0.02 g h^{-1}, while water loss associated with electrolysis and electro-osmotic transport was 0.40 ± 0.01 g h^{-1} (**Fig. 2a**). Increasing the pressure to 3 bar effectively eliminated osmotic water crossover, leaving only 0.21 ± 0.01 g h^{-1} of water loss attributable to electrolysis and electro-osmotic drag. The cell voltage, however, exhibited pronounced fluctuations when a back pressure of ~3 bar was applied, indicating that the influence of additional back pressure on the MEA system requires further systematic investigation in future studies (**Fig. S10**).

Based on the van't Hoff relation for the bulk electrolyte concentrations, a pressure difference of ~28 bar would be required to fully counterbalance the osmotic pressure. However, accounting for Donnan exclusion within the BPM significantly reduces the effective osmotic driving force, such that a pressure difference of approximately 3 bar may be sufficient to suppress osmotic water transport (**Supplementary Note 1**). Under reverse-bias operation, residual water loss persists due to ion flux generated by WD and the

electro-osmotic drag with multiple ionic species, suggesting that a larger pressure difference would be required to mitigate these transport processes.

Based on the water-loss values in **Fig. 2b**, we developed a simplified steady-state water-flux model based on water transport within the BPM (**Supplementary Note 2**). This semi-quantitative model captures the water-loss behaviour observed in **Fig. 2b** and is supported by CEL-thickness-dependent water-transport experiments. In the pure-water catholyte/pure-water anolyte system, the anolyte water loss increased with increasing CEL thickness, consistent with the reduced diffusive transport of water to the junction from the catholyte to feed the dissociation reaction, and thus an increasing fraction coming from the anolyte. In the 0.50 M NaCl catholyte/pure-water anolyte system, the anolyte water loss decreased as the CEL thickness increased (**Fig. S11** and **Table S1**), consistent with a regime where the activity driven osmosis of water is significant (see **Supplementary Note 2** for detailed discussion). The measured Cl^- crossover rate at 0.50 A cm^{-2} was only ~20 μmol cm^{-2} h^{-1}, corresponding to ~0.11% of the applied current on a charge-equivalent basis (**Fig. S12**). Thus, water-transport with hydrated Cl^- cannot significantly contribute to the net water flux. The electro-osmotic contribution is thus primarily attributed to H^+ and OH^- transport generated by BPM water dissociation.

Under the condition that minimizes (electro)osmotic transport (0.50 M NaOH anolyte and 0.50 M NaCl catholyte), we conducted a 120-h test at 0.50 A cm^{-2}, using a catholyte volume of 1.0 L and an anolyte volume of 100 mL. The system exhibited a degradation rate of 2.6 mV h^{-1}, comparable to values reported in the literature for electrodeposited Co-based catalysts operating in alkaline electrolytes.[30–32] After 120 h of operation, the net anolyte water consumption, after subtracting evaporation losses, was measured to be 0.166 g h^{-1}, similar to the theoretical electrolysis-driven water consumption of 0.168 g h^{-1}. These results suggest that water loss associated with (electro)osmosis is effectively suppressed, an important result for the steady-state operation of such a system.

Under reverse-bias operation, the Na^+ ions in the anolyte are expected to migrate toward the catholyte via an electric field–driven mechanism, while Cl^- ions in the catholyte tend to move toward the anolyte under the combined driving forces of the electric field and the concentration gradient. Under these conditions, the net water transport associated with ion migration appears to be nearly balanced, resulting in minimal overall water crossover. However, like pure-water-fed BPMWE systems, water loss induced by electrolysis predominantly occurred in the anolyte compartment. This phenomenon is attributed to the imbalance in the amount of water dragged by H^+ and OH^- ions generated through WD, leading to asymmetric water transport between the two compartments. Despite the opposing migration of Na^+ and Cl^- ions and the relatively small anolyte volume (100 mL), the anolyte pH remained nearly unchanged at approximately 13.5 after 120 h of operation at 500 mA cm^{-2}. Furthermore, *N*,*N*-diethyl-p-phenylenediamine (DPD) analysis confirmed that no measurable free chlorine was generated under these conditions.

Overall, these results show that electrolyte balancing and modest catholyte back-pressure can substantially suppress water redistribution in the asymmetric BPM electrolyzer, thereby narrowing one source of time-dependent evolution in interfacial chemical gradients. In future work, careful electrolyte engineering will be key to identifying the optimal operating window that simultaneously maximizes catalytic performance, suppresses the ClER, and minimizes the required NaOH concentration.

Chlorine evolution limits the BPM seawater electrolyzer durability

To evaluate the impact of catholyte composition on stability, we conducted durability tests at 0.50 A cm^{-2} for 20 h. The BPM electrolyzer was operated with a pure-water anolyte, while the catholyte composition was systematically varied. As shown in **Fig. 3a**, electrolyzers operated with NaCl or HCl catholytes exhibited rapid degradation rates exceeding 60 mV h^{-1}, whereas the Na_2SO_4 system showed a degradation rate of 8.7 mV h^{-1}. In contrast, BPM systems employing NaOH or pure water as the catholyte maintained nearly constant voltage throughout the test duration. Monitoring the anolyte pH during operation showed that the NaCl, Na_2SO_4, and HCl systems all experienced comparable anolyte acidification, reaching pH ~3 after 20 h (**Fig. 3b**). By contrast, the anolyte pH remained stable in the case of NaOH in the catholyte, indicating negligible Na^+ transport into the anolyte and suggesting that electric field-driven ion migration dominates over concentration gradient-driven diffusion. Notably, although the Na_2SO_4 system exhibited a similar anolyte acidification trend to the NaCl and HCl systems, its degradation rate was substantially lower. This discrepancy indicates that Cl^- crossover, rather than acidification alone, is a key driver of system degradation. Consistent with this interpretation, DPD

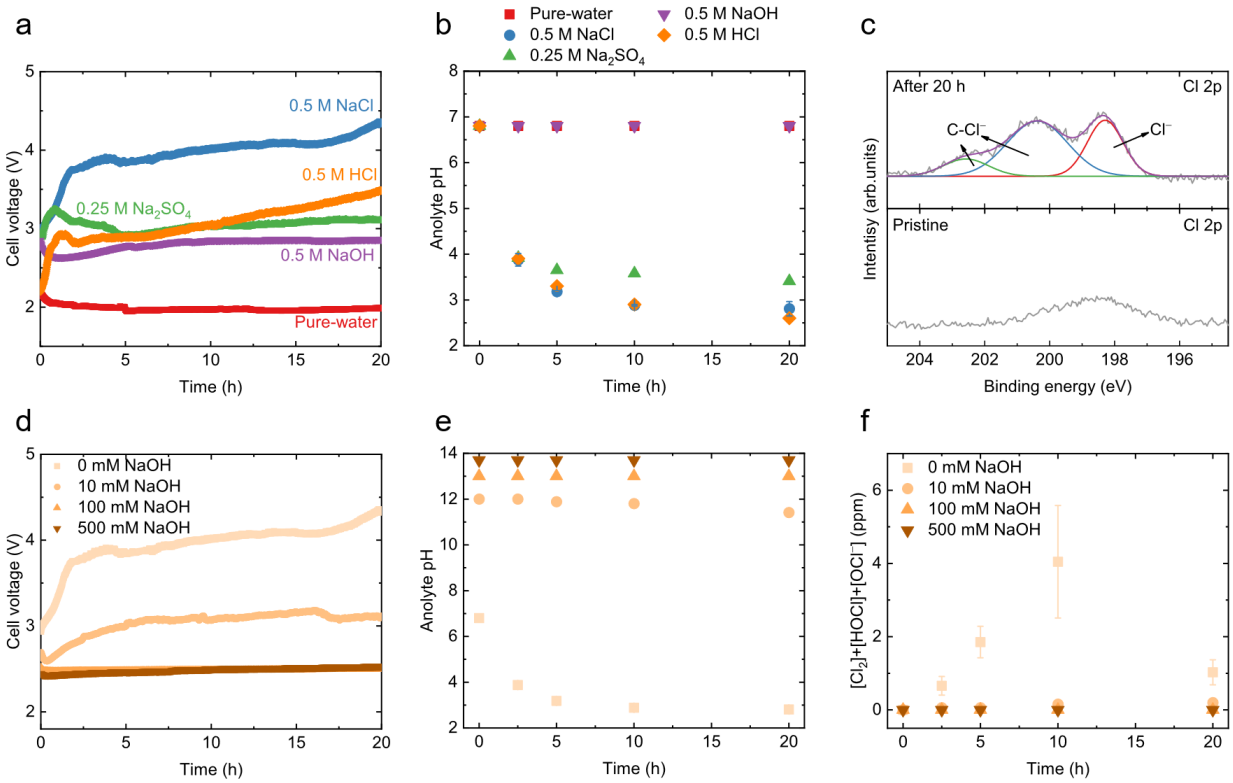

Fig. 3. **Degradation of BPM electrolyzers induced by the ClER.** Time-dependent variations in (a) cell voltage and (b) anolyte pH for the BPM electrolyzers during operation at 0.50 A cm^{-2} and 60 °C using different catholytes. (c) XPS Cl 2p spectra of the anode catalysts before and after a 20 h durability test using 0.5 M NaCl catholyte. Time-dependent variations in (d) cell voltage, (e) anolyte pH, and (f) total chlorine concentration for the BPM electrolyzer operated with a 0.50 M NaCl catholyte and varying NaOH concentrations at the anode.

analysis confirmed the generation of free chlorine of ~1 ppm in both the NaCl and HCl systems after the durability tests (**Fig. S13**).

Chlorine generated via ClER is a strong oxidizing agent and known to be a key cause of electrolyzer degradation due to its detrimental effects on both the AEL and electrocatalysts.[33–35] X-ray photoelectron spectroscopy (XPS) analysis revealed the formation of C–Cl covalent bonding on both the anode catalyst and the AEL after 20 h of operation in the NaCl system (**Fig. 3c** and **S14**), along with an increased proportion of oxidized carbon species (**Fig. S15**). These observations suggest that, consistent with a previous study, chemical reactions with free chlorine led to the formation of new bonds, resulting in structural degradation.[22] Moreover, Raman spectroscopy revealed substantial changes in both the peak positions and intensities of the Co-based catalyst after 20 h of operation, further supporting ClER-induced structural degradation (**Fig. S16**).

To quantitatively correlate ClER with degradation rates, we varied the NaOH concentration in the anolyte while using 0.50 M NaCl as the catholyte. Because alkaline conditions inhibit the ClER, numerous studies have added concentrated NaOH or KOH (≥1 M) to seawater during operation.[19,36–38] The initial performance of BPM electrolyzers increased with NaOH concentration (**Fig. S17**). The system stability also increased with the NaOH concentration. At an anolyte concentration of 10 mM NaOH, the degradation rate was reduced to approximately 22 mV h^{-1}. Increasing the NaOH concentration to 100 mM or higher eliminated apparent degradation (**Fig. 3d**). Correspondingly, anolyte pH measurements showed a decrease from an initial value of 12 to 11.4 after 20 h for the 10 mM NaOH system, whereas systems containing ≥100 mM NaOH maintained their initial pH throughout operation (**Fig. 3e**). After 20 h, the accumulated free chlorine concentration was ~0.2 ppm for the 10 mM NaOH system, corresponding to a Faradaic efficiency of ~0.0006%, while no detectable ClER occurred at NaOH concentrations of 100 mM (**Fig. 3f**). The gradual decrease in total chlorine concentration after the initial accumulation period likely reflects the instability of free chlorine species under electrolysis conditions, where chlorine-containing species can undergo further chemical transformations or be released as gaseous products, consistent with a previous report.[15]

To investigate the reversibility of ClER-induced degradation, we conducted an additional experiment in which NaOH salts were introduced into the anolyte after operation in a system employing 0.50 M NaCl as the catholyte and pure-water as the anolyte. When NaOH was added to the pure-water anolyte of a BPM electrolyzer system whose cell voltage had risen to ~3.9 V owing to the 0.50 M NaCl catholyte, the cell voltage rapidly decreased to ~2.9 V and subsequently stabilized (**Fig. S18**). Nevertheless, in comparison to a system employing a 0.50 M NaOH anolyte that maintained stable operation at ~2.5 V (**Fig. S17**), the observed behavior suggests that ClER-induced degradation is irreversible. This conclusion is further supported by EIS analysis, which revealed a significant increase in the high-frequency ohmic resistance after operation (**Fig. S18**).

Overall, these results suggest a direct correlation between the occurrence of the ClER and the degradation of the BPM electrolyzer, indicating that even trace levels of ClER can induce relevant performance deterioration. However, this degradation can be effectively suppressed by maintaining sufficient local OH^- availability at the anode to suppress chlorine chemistry.

Enhancing the local anodic pH to suppress the ClER

Based on the above insights, we hypothesized that minimizing the distance between the AEL and the anode would increase the local anodic pH, thereby suppressing the ClER. In pure-water-fed anode configurations, OH^- is supplied solely via WD within the BPM, giving rise to a pronounced OH^- concentration gradient into the anode away from the membrane.[39] When the local pH falls below ~11 further from the AEL, the OER pathway begins to shift from an alkaline ($4OH^- \rightarrow O_2 + 2H_2O + 4e^-$) to an acidic mechanism ($2H_2O \rightarrow O_2 + 4H^+ + 4e^-$), resulting in localized proton generation.[40,41] This results in both catalyst degradation and voltage increases. Accordingly, in conventional electrodeposited porous transport layer (E-PTL) configurations, catalysts positioned far from the AEL are exposed to locally acidified environments that may favor the ClER (**Fig. 4a**, left).[40,42] Moreover, the rapid decrease of the bulk anolyte pH to ~4 within 2.5 h under chloride-containing operation (**Fig. 3b**) suggests the formation of acidic anode microenvironments in which ClER becomes increasingly competitive.

To overcome these limitations, we directly electrodeposited the anode catalyst on the AEL, thereby concentrating the catalytic sites in proximity to the membrane. This configuration is expected to enable the OER to occur under a more-alkaline local environment, suppressing ClER (**Fig. 4a**, right). To this end, we developed an electrodeposited membrane–electrode assembly (E-MEA) configuration (**Fig. S19**) and optimized the electrodeposition current density and precursor-solution composition (**Figs. S20–S23**). Under optimized conditions, the successful formation of a Co-based catalyst on the AEM was confirmed by SEM, energy-dispersive X-ray spectroscopy (EDS), XPS, and Raman spectroscopy (**Figs. 4b** and **S24-S26**).[31,32,43,44] In E-PTL, a Co nanosheet architecture was formed on the Ti fibers, whereas in E-MEA, a CoO_x layer developed at the AEL/PTL interface, with a substantial amount of CoO_x also deposited within the inter-fiber regions of the Ti-based substrate (**Fig. S27**). The

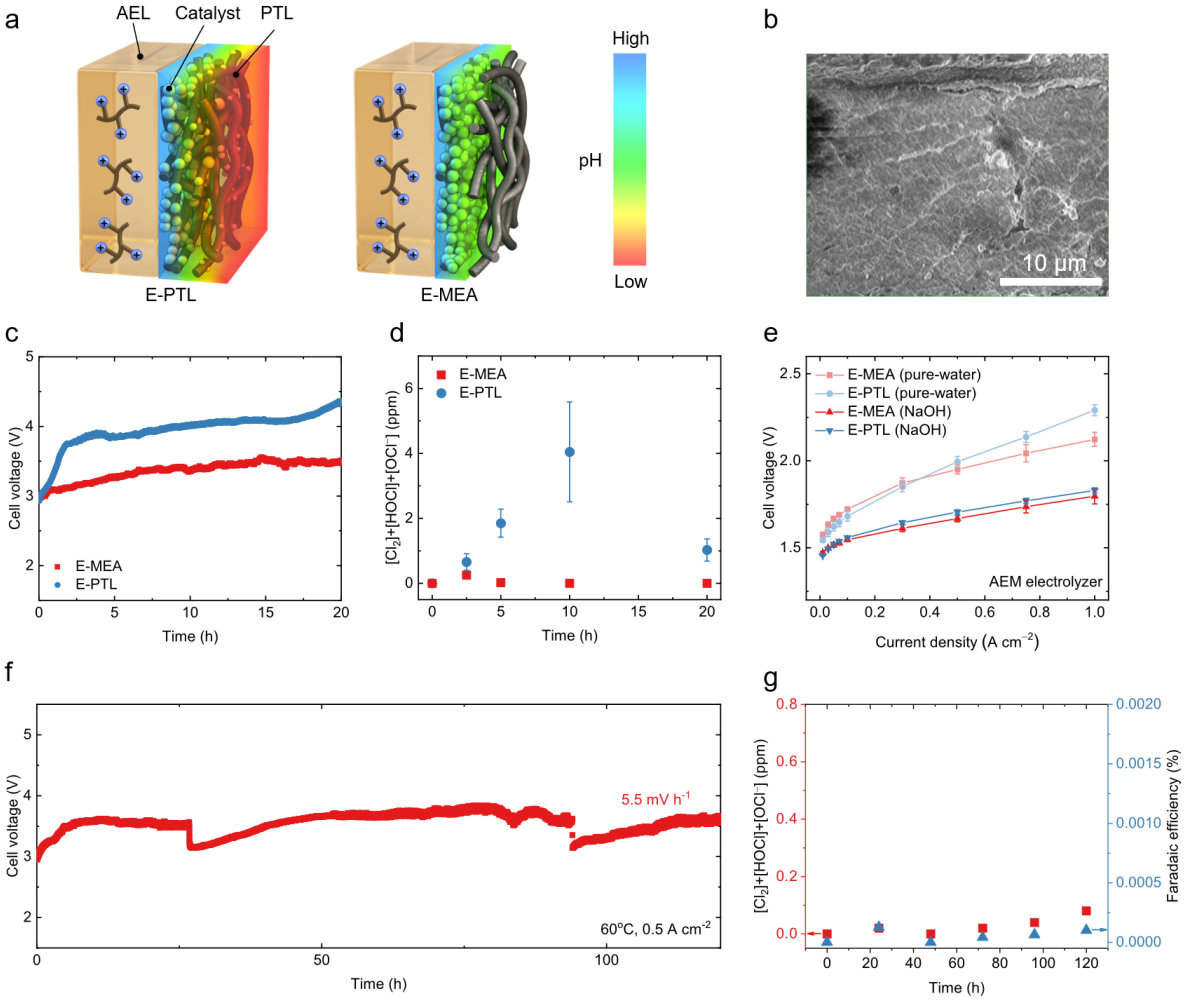

Fig. 4. Enhancing durability of BPM electrolyzers via local pH gradient modulation at the anode. (a) Schematic comparison of local pH gradients in E-PTL and E-MEA configurations. The pH gradient is color-coded, with lower pH values shown in red and higher pH values in blue. (b) SEM image of the Co-based catalyst synthesized on the AEL (E-MEA). (c) Time-dependent cell voltage and (d) total chlorine concentration for E-MEA and E-PTL configurations during operation at 0.5 A cm^{-2} and 60 °C in BPM electrolyzers using 0.5 M NaCl catholyte and pure-water anolyte. (e) Polarization curves of E-MEA and E-PTL configurations in AEM electrolyzers operated at 60 °C using NaOH or pure-water as the anolyte. (f) Cell voltage and (g) total chlorine concentration and Faradaic efficiency for the ClER as a function of time during operation at 0.5 A cm^{-2} and 60 °C in the BPM electrolyzers with 0.50 M NaCl catholyte and pure-water anolyte.

CoO_x loadings were 4.5 ± 0.9 mg cm^{-2} and 6.5 ± 1.1 mg cm^{-2} for the E-MEA and E-PTL configurations, respectively. Cross-sectional SEM–EDS analysis showed that CoO_x was electrodeposited throughout a ~115 µm-thick region in the E-PTL, whereas in the E-MEA, CoO_x was distributed within a ~42 µm region extending from the AEL (**Fig. S28**). These results indicate that, in the E-MEA, CoO_x is more densely concentrated in a region closer to the MEA compared to the E-PTL. Because electrodeposition was performed with the same total charge for both E-PTL and E-MEA, these observations indicate that a denser catalyst layer preferentially formed near the AEL side in the E-MEA. When tested in a NaCl catholyte/pure-water anolyte system, the E-MEA BPM electrolyzer achieved 0.50 A cm^{-2} at ~2.8 V and exhibited more than a threefold reduction in the degradation rate during 20 h of operation at 0.50 A cm^{-2} (**Fig. 4c**). Furthermore, the total free chlorine concentration remained below 0.02 ppm after 20 h (**Figs. 4d** and **S29**). Although the E-MEA places the catalyst in closer proximity to the AEL, the resulting increase in local pH substantially suppresses ClER, thereby reducing the overall exposure of the membrane to reactive chlorine species.[19] Water-transport measurements of the E-MEA revealed a water loss comparable to that of the E-PTL under a 0.50 M NaCl catholyte with pure-water anolyte configuration (**Fig. S30**). This observation suggests that the E-MEA architecture does not significantly affect the intrinsic water-transport properties of the AEL, such as water uptake, water activity, and water chemical potential.

To study the difference in local anodic pH between the E-MEA and E-PTL configurations, we compared their performance in an AEM electrolyzer using NaOH or pure-water as the anolyte. In pure-water-fed AEM electrolyzers, local pH gradients can develop from the balance between OH^- transport from the cathode through the AEL and OH^- consumption by the anodic reaction, making this configuration useful for probing the relationship between catalyst architecture and local pH gradients. While both systems showed comparable performance in NaOH, pronounced differences emerged at high current densities under pure-water conditions (**Fig. 4e**). In NaOH electrolytes, no significant differences in η_s or kinetic overpotential (η_{kin}) were observed at 1.0 A cm^{-2} (**Fig. S31**). However, in pure-water electrolytes, the E-MEA system exhibited approximately 80 mV lower η_s and 110 mV lower η_{res} than the E-PTL system (**Fig. S32**). These results indicate that the observed performance differences are most consistent with variations in the local pH gradient rather than intrinsic catalytic activity alone. Additionally, under pure-water conditions at low current densities (<300 mA cm^{-2}), the performances of the two systems were nearly identical, consistent with previous reports that pH gradients become increasingly severe at higher current densities.[45,46] In addition, the E-MEA configuration outperformed the E-PTL configuration in pure-water-fed BPM electrolyzers (**Fig. S33**). The E-MEA system exhibited improved durability, maintaining a voltage decay rate of 0.03 mV h^{-1} at a current density of 0.5 A cm^{-2} over 600 h.

The durability of the E-MEA system was evaluated at 0.50 A cm^{-2} in a 0.50 M NaCl system, where it demonstrated a degradation rate of 5.5 mV h^{-1} over 120 h (**Fig. 4f**). This enhanced durability is consistent with ClER suppression, with the Faradaic efficiency for ClER remaining below 0.0001% throughout the test duration (**Fig. 4g**). Most of the degradation occurred within the initial 10 h, after which the system exhibited a degradation rate of 0.46 mV h^{-1} from 10 to 120 h. EIS measurements revealed negligible ohmic and WD resistance changes between 20 h and 120 h of operation (**Fig. S34**). Together with the EIS results, this behavior suggests rapid initial degradation of the water dissociation catalyst and interfacial region, followed by the establishment of a relatively stable operating state. Raman analysis showed that, after 120 h of operation, the E-MEA system retained cobalt (oxy)hydroxide structures on both the AEL and PTL sides that were comparable to those observed prior to operation (**Fig. S35**). SEM images showed that the post-operation morphology remained similar to the initial state (**Fig. S36**), and EDS indicated that the CoO_x layer on the AEL side was well preserved despite partial agglomeration (**Fig. S37**). Notably, XPS analysis revealed that the C–Cl signal after 120 h of operation in the E-MEA system was less pronounced than that observed after 20 h of operation in E-PTL (**Fig. S38**), suggesting more effective suppression of ClER. These results collectively indicate that the enhanced durability of E-MEA can be attributed to suppression of local anodic pH gradients and the associated ClER pathway.

The performance and durability demonstrated in this work remain below those of state-of-the-art PEM electrolyzers, which typically exhibit degradation rates on the order of a few µV h^{-1} over thousands of hours of operation. Practical commercial deployment of seawater, or other impure-water, electrolyzers would probably need to match this performance, given the low cost of water purification by reverse osmosis.[47] However, for some applications, like H_2 generation in remote operations or for expeditionary operations,[48,49] robustness provided by this design may be advantageous.

Beyond seawater electrolysis, this work furthers the understanding of local pH gradients that emerge during impure-water electrolysis and presents effective strategies to mitigate their impact. Given that similar local pH gradients are expected in a broad range of electrochemical systems involving complex feed streams, including CO_2 electrolysis,[45] organic oxidation and reduction reactions,[50] electrochemical carbon capture,[51] electrodialysis,[52] and other ion-transport-driven processes, the insights developed herein may provide broadly applicable design principles for next-generation electrochemical technologies operating under non-ideal feed conditions.

Conclusions

In summary, we elucidate the origin and consequences of local pH gradients in a BPM electrolyzer operated with a 0.50 M NaCl catholyte and a pure-water anolyte, and overcome these limitations through CCM (cathode) and E-MEA (anode) architectures. The presence of NaCl induces pronounced pH gradients at the cathode–CEL interface, leading to significant voltage losses; these effects are shown to be partially mitigated by the CCM configuration. More critically, partial Cl^- crossover combined with locally acidic environments promotes the ClER, which compromises the durability of conventional BPM electrolyzers. At the anode, minority Cl^- crossover becomes especially detrimental when local OH^- delivery is insufficient, enabling the ClER and accelerating degradation in conventional BPM architectures. By directly electrodepositing the anode onto the AEL, the E-MEA architecture suppresses chlorine-related degradation and improves durability. The optimized E-MEA system exhibits a degradation rate of 5.5 mV h^{-1} during 120 h of operation at 0.50 A cm^{-2}, while reducing the Faradaic efficiency of ClER to approximately 0.0001%. Overall, these results show that controlling local pH gradients is central to improving the performance and durability of impure-water asymmetric BPM

electrolyzers. Furthermore, it demonstrates that high durability can be achieved using an ionomer-free Co-based anode in this BPM architecture.

One challenge that remains with this BPM system design involves undesired water consumption by means of the anolyte, consisting of purified electrolyte rather than seawater. In a system employing 0.50 M NaCl as the catholyte and pure-water as the anolyte, we observed an anolyte water consumption rate of approximately 0.78 g h^{-1}. We were able to reduce anolyte water consumption to approximately 0.25 g h^{-1} either by adjusting the anolyte salt concentration to match that of the catholyte or by applying a pressure of ~3 bar to the catholyte feed. Future work should therefore combine electrolyte engineering, pressure control, ion-crossover blocking, and direct quantification of local chemical gradients under impure-water conditions to define the steady-state practical operating window of asymmetric BPM electrolyzers. Understanding and controlling degradation in impure-water is further relevant for suppressing impurity-related degradation modes in nominally electrolyte free systems.[10]

Materials and methods

Anode catalyst preparation. The electrodeposited porous transport layer (E-PTL) catalyst employed as a model system in this study was synthesized via electrodeposition in a conventional three-electrode configuration. A Pt–Ti gas diffusion layer (Pt–Ti PTL; electrochemically platinized titanium fiber felt, Fuel Cell Store) was used as the working electrode, with a Pt foil as the counter electrode and a saturated calomel electrode (SCE) as the reference electrode. Electrodeposition was carried out in an aqueous electrolyte containing 250 mM $CoCl_2$ (99.9%, Sigma-Aldrich). A constant current density of −60 mA cm^{-2} was applied for 10 min. After deposition, the electrode was thoroughly rinsed with pure-water and dried in an oven at 40 °C for at least 20 min prior to use. The electrodeposited membrane–electrode assembly (E-MEA) was fabricated via in situ electrodeposition within a MEA configuration. An HQPC-TMA anion-exchange membrane (50 µm, IEC = 2.4) was sandwiched between a Pt–Ti PTL cathode and a stainless-steel felt anode (316 SS, 10AL3, Bekaert) to form an AEM electrolyzer. During electrodeposition, a 250 mM $CoCl_2$ solution was supplied to the cathode compartment, while a 250 mM NaOH solution was delivered to the anode compartment at a flow rate of approximately 20 mL min^{-1}. A current density of −60 mA cm^{-2} was applied for 10 min. Following electrodeposition, the MEA was disassembled, and both the Pt–Ti PTL and the AEL were thoroughly rinsed with pure-water before further use. For proton exchange membrane (PEM) electrolyzer experiments, an IrO_2-based anode catalyst was prepared by spray coating onto a Pt–Ti PTL substrate. The anode ink was prepared in a solution containing 0.10 g of core–shell Ir/IrO_x catalyst (Fuel Cell Store), 0.50 g of pure-water, 1.70 g of isopropyl alcohol (IPA), and 0.20 g of 5wt% Nafion solution. The ink was sonicated until a homogeneous dispersion of nanoparticles was achieved. The Pt–Ti PTL substrate was cut into a 5 cm × 5 cm square and fixed onto a hot plate maintained at 90 °C. The catalyst loading was approximately 2.0 mg cm^{-2}. For ionomer top-coating tests, Co-based catalysts electrodeposited on Pt–Ti PTLs were spray-coated with either a 5 wt% Nafion solution, a 5 wt% PiperION ionomer suspension (TP-85, Versogen), or a 5 wt% HQPC–TMA ionomer. The ionomer loading was controlled at 1.0 mg cm^{-2}.

To determine the Co-based catalyst loading in the E-PTL and E-MEA configurations, we measured the mass difference before and after catalyst electrodeposition. For the E-PTL, the Pt–Ti PTL was weighed before electrodeposition and then reweighed after electrodeposition and drying in an oven at 65 °C for at least 1 h. The mass loading of the electrodeposited Co-based catalyst was 6.5 ± 1.1 mg cm^{-2}. For the E-MEA, the Pt–Ti PTL and HQPC-TMA AEL were first thoroughly dried and weighed, followed by electrodeposition. The electrodeposited sample was then dried under the same conditions, at 65 °C for at least 1 h, before being weighed again. The resulting CoO_x loading was 4.5 ± 0.9 mg cm^{-2}.

Cathode catalyst preparation. The cathode was made by spraying a Pt catalyst ink onto Toray Carbon Paper (wet-proofed, Fuel Cell Store) to achieve a 2.0 mg cm^{-2} loading. The cathode catalyst ink consisted of 0.18 g of Pt black (high SA, Fuel Cell Store), 3.3 g of pure-water, 10.4 g of IPA, and 0.9 g of 5wt% Nafion solution. The carbon paper substrate was cut into a 5.5 cm × 5.5 cm square and fixed onto a hot plate maintained at 90 °C for spray-coating. For the fabrication of the CCM, a Nafion 212 membrane (50 µm thick) was cut into 1.5 × 1.5 cm^2 pieces and fixed onto a glass slide using adhesive tape. The membrane was placed on a hot plate maintained at 90 °C, and the same catalyst ink was spray-coated onto the membrane to achieve a catalyst loading of approximately 2 mg cm^{-2}.

For AEM electrolyzer experiments, the cathode catalyst ink consisted of 0.18 g of Pt black, 3.3 g of pure-water, 10.4 g of IPA, and 0.90 g of 5 wt% PiperION ionomer suspension. The carbon paper substrate was cut into a 5 cm × 5 cm square for a loading amount of 2.0 mg cm^{-2} and fixed onto a hot plate maintained at 90 °C for spray-coating.

Preparation of the WD catalyst. The SnO_2 WD catalyst was prepared following the procedure reported in our previous work.[24] Briefly, a Nafion-based cation exchange layer (CEL, 1.5 cm^2) was placed on a slide glass, carefully wiped to remove trapped air bubbles, secured with paper tape, and positioned on a hot plate maintained at 90 °C. A 50 mM $SnCl_4$ solution (98%, Sigma-Aldrich) was then spray-coated onto the CEL. The SnO_2 catalyst loading was controlled to be 70 µg cm^{-2}.

BPM Electrolyser fabrication and measurements. Nafion NR212 (50 µm) and HQPC-TMA (50 µm) were employed as the CEL and AEL, respectively, in the BPMs. Prior to use, the CEL was soaked and stored in pure-water. The AEL was stored in 1 M KOH and thoroughly rinsed with pure-water immediately before cell assembly. Both the anode and cathode were fabricated with an active area of 1.0 cm^2. The electrolyzer cell was assembled using a torque wrench, with all bolts tightened to 4.0 N·m.

Electrolytes preheated to 60 °C were supplied to both the anode and cathode compartments at a flow rate of 30 mL min^{-1}. Electrochemical measurements were initiated after the cell temperature stabilized at 60 ± 2°C with minimal fluctuation, using a BioLogic VSP-300 potentiostat. Pure-water or NaOH solutions with concentrations ranging from 10 to 500 mM (98%, Sigma-Aldrich) were used as the anolyte. The catholytes studied included 0.5 M NaCl (99%, Sigma-Aldrich), 0.25 M Na_2SO_4 (99%, Sigma-Aldrich), 0.5 M NaOH, 0.5 M HCl (37%, Sigma-Aldrich), and pure-water, depending on the experimental conditions.

Polarization measurements were conducted by initially holding the current density at 10 mA cm^{-2} for 30 s, followed by incremental increases of 20 mA cm^{-2} from 10 to 70 mA cm^{-2} and 100 mA cm^{-2} increments from 100 to 500 mA cm^{-2}, with each step maintained for 30 s. The current density was then held at 0.50 A cm^{-2} for 5.0 min before stepping down in reverse order. The cell voltage was recorded

at each step, and polarization curves were constructed using the average voltage measured during the final second of each current step. Electrochemical impedance spectroscopy (EIS) measurements were performed at a current density of 0.50 A cm^{-2} using an AC perturbation amplitude of 6% of the applied DC current. The frequency range was scanned from 600 kHz to 1 Hz with 10 points per decade. The ohmic and water-dissociation resistances were obtained from EIS analysis by fitting the spectra using Bio-Logic EC-Lab software (version 11.52). The x-intercept was assigned to the ohmic resistance, while the resistance of the first semicircle was assigned to water dissociation resistance, consistent with our previous analysis.[6] The corresponding overpotentials were calculated by multiplying each resistance by the applied current density of 0.50 A cm^{-2}. The residual overpotential was then obtained by subtracting η_s and η_{wd} from the total overpotential. Durability tests were conducted at a constant current density of 0.50 A cm^{-2}, with the cell voltage recorded at 1.0 min intervals. The pH of the anolyte was measured via the 6367S-10D pH meter (Horiba). The Na^+ and Cl^- crossovers were both measured via the pH meter and ion chromatography (Thermo Fisher Dionex ICS-6000).

Materials characterization. Raman measurements were performed using the inVia confocal Raman microscope (Renishaw), using a 532 nm excitation laser with 10% laser power. Spectral calibration was carried out using the characteristic Raman band of silicon at 520.8 cm^{-1}. All spectra are presented using the same raw intensity scale to enable direct comparison of relative peak intensities between samples. Scanning electron microscopy (SEM) analyses were conducted on a FEI Quanta FEG 250 instrument fitted with an energy-dispersive X-ray spectroscopy (EDX) detector (Bruker XFlash 7) for elemental characterization. X-ray photoelectron spectroscopy (XPS) measurements were obtained using a Kratos Axis Ultra DLD system with a monochromatic Al Kα radiation source operated at a pass energy of 20 eV. All binding energies were referenced to the C 1s peak, which was set to 284.8 eV.

Free chlorine concentration measurements. The total free chlorine concentration in the anolyte was measured using N, N-diethyl-p-phenylenediamine (DPD) method at 530 nm with a spectrophotometer (DR 900, HACH Co., USA). The current efficiency for the chlorine evolution reaction (ClER) was calculated by following equation.

$$\text{Faradaic Efficiency}(\%) = \frac{C \times V \times n \times F}{I \times t} \times 100$$

Where C is the concentration of free chlorine (mol L−1), V is volume (L), n is the number of electron transfer (2 eq mol-1), F is the Faraday constant (96485 C mol-1), I is the applied current (A), and t is the electrolysis time (s).

Water transport measurements. To quantify water transport in BPM electrolyzers, changes in the water content of the anolyte and catholyte were separately evaluated by distinguishing the contributions from evaporation, osmosis, electro-osmosis, and water electrolysis. All experiments were conducted at 60 °C for 20 h using an electrolyte volume of 200 mL, and the water change was normalized and reported in units of g h^{-1}. Evaporative water loss was determined by measuring the time-dependent volume decrease of pure-water, 0.10 M NaOH, 0.50 M NaOH, and 0.50 M NaCl solutions under static conditions without pump circulation. The densities of pure-water, 0.10 M NaOH, 0.50 M NaOH, and 0.50 M NaCl at 60 °C were taken as 0.983, 0.986, 1.002, and 1.001 g mL^{-1}, respectively, and were used to convert volume changes to mass losses. Osmotic water transport was investigated by circulating both anode and cathode electrolytes in the BPM electrolyzer under open-circuit voltage (OCV) conditions and monitoring the time-dependent volume change of each compartment. Water transport due to electroosmosis and water electrolysis was evaluated by measuring the volume change before and after operation at 500 mA cm^{-2} under various anolyte and catholyte conditions. The combined contribution of electrolysis and electro-osmosis was determined by subtracting the evaporative and osmotic water loss from the total measured water change.

For the pressurization experiment, the catholyte outlet of the MEA cell was connected to a needle valve to regulate the pressure. The catholyte flow rate was fixed at 120 mL min^{-1}, and the outlet pressure was controlled by adjusting the degree of closure of the needle valve. During the tests, an additional pressure of 1.5 bar or 3.0 bar was applied to the catholyte side relative to the anolyte side. A 0.50 M NaCl solution was used as the catholyte, while pure-water was used as the anolyte. The change in anolyte volume was measured before and after operation at 500 mA cm^{-2} at 60 °C.

Author contributions

S.H. and S.W.B. designed the study, analysed the data, and wrote the manuscript. S.H. performed most experiments and catalyst synthesis. G.H.C. and D.X. supported BPM experiments and data analysis. W.Z. performed Raman spectroscopy and SEM analyses. D.S. performed XPS measurements. J.S. and T.F.J. provided intellectual advisement and manuscript editing. J.Y.L. synthesized HQPC-TMA membranes and ionomers. J.R. and S.W.B. supervised the project. All authors participated in and contributed to the final version.

Conflicts of interest

There are no conflicts to declare.

Acknowledgements

The studies of the effect of catalyst structure on ionic and reaction water dissociation resistances in the BPM and the BPM electrolyzer testing were supported by the US Office of Naval Research (grant N00014-24-1-2433). J.R. acknowledges the National Research Foundation of Korea grant funded by the Korea government (MSIT) (RS-2024-00348577, RS-2024-00415940, RS-2024-00449579, and RS-2024-00399165), the Institute for Basic Science (IBS-R006-D1), and the Creative-Pioneering Researchers Program (0458-20240094) through Seoul National University.

References

1 J. C. Bui, E. W. Lees, D. H. Marin, T. N. Stovall, L. Chen, A. Kusoglu, A. C. Nielander, T. F. Jaramillo, S. W. Boettcher, A. T. Bell and A. Z. Weber, *Nat. Chem. Eng.*, 2024, **1**, 45–60.

2 C. G. Rodellar, J. M. Gisbert-Gonzalez, F. Sarabia, B. Roldan Cuenya and S. Z. Oener, *Nat. Energy*, 2024, **9**, 548–558.

3 K. V. Petrov, C. I. Koopman, S. Subramanian, M. T. M. Koper, T. Burdyny and D. A. Vermaas, *Nat. Energy*, 2024, **9**, 932–938.

4 W. L. Toh, H. Q. Dinh, A. T. Chu, E. R. Sauvé and Y. Surendranath, *Nat. Energy*, 2023, **8**, 1405–1416.
5 S. Z. Oener, M. J. Foster and S. W. Boettcher, *Science.*, 2020, **369**, 1099–1103.
6 L. Chen, Q. Xu, S. Z. Oener, K. Fabrizio and S. W. Boettcher, *Nat. Commun.*, 2022, **13**, 3846.
7 A. W. Tricker, J. K. Lee, F. Babbe, J. R. Shin, A. Z. Weber and X. Peng, *ACS Energy Lett.*, 2023, **8**, 5275–5280.
8 E. Lucas, J. C. Bui, T. N. Stovall, M. Hwang, K. Wang, E. R. Dunn, E. Spickermann, L. Shiau, A. Kusoglu, A. Z. Weber, A. T. Bell, S. Ardo, H. A. Atwater and C. Xiang, *ACS Energy Lett.*, 2024, **9**, 5596–5605.
9 T. Gao, L. Schulte, L. Xiao, E. Yamamoto, A. S. Metlay, C. J. Sheehan, S. Marth, H. Park, S. Sasmal, F. J. Galang, C. Bae, A. Z. Weber, S. W. Boettcher and T. E. Mallouk, *Adv. Energy Mater.*, 2025, **15**, 2404285.
10 G. A. Lindquist, Q. Xu, S. Z. Oener and S. W. Boettcher, *Joule*, 2020, **4**, 2549–2561.
11 Y. Lei, J. Dong, Z. Peng, L. Wang, J. Chen and D. Yan, *Chem. Commun.*, 2025, **61**, 9169–9187.
12 E. Hong, Z. Yang, H. Zeng, L. Gao and C. Yang, *ACS Mater. Lett.*, 2024, **6**, 1623–1648.
13 A. H. Faqeeh and M. D. Symes, *Electrochim. Acta*, 2024, **493**, 144345.
14 S. Adisasmito, K. Khoiruddin, P. D. Sutrisna, I. G. Wenten and U. W. R. Siagian, *ACS Omega*, 2024, **9**, 14704–14727.
15 D. H. Marin, J. T. Perryman, M. A. Hubert, G. A. Lindquist, L. Chen, A. M. Aleman, G. A. Kamat, V. A. Niemann, M. B. Stevens, Y. N. Regmi, S. W. Boettcher, A. C. Nielander and T. F. Jaramillo, *Joule*, 2023, **7**, 765–781.
16 G. P. Vergel, H. Mu, N. Kolobov, J. Biemolt, D. A. Vermaas and T. Burdyny, *Nat. Chem. Eng.*, 2025, **2**, 676–684.
17 D. Xi, A. M. Alfaraidi, J. Gao, T. Cochard, L. C. I. Faria, Z. Yang, T. Y. George, T. Wang, R. G. Gordon, R. Y. Liu and M. J. Aziz, *Nat. Energy*, 2024, **9**, 479–490.
18 M. F. Rochow, D. H. Marin, H. J. Cassady, R. T. Hannagan, K. Yan, J. T. Perryman, A. C. Nielander, T. F. Jaramillo and M. A. Hickner, *ACS Electrochem.*, 2025, **1**, 1812–1820.
19 Y. Liu, Y. Wang, P. Fornasiero, G. Tian, P. Strasser and X.-Y. Yang, *Angew. Chemie Int. Ed.*, 2024, **63**, e202412087.
20 J. H. Han, E. Jwa, H. Lee, E. J. Kim, J. Y. Nam, K. S. Hwang, N. Jeong, J. Choi, H. Kim, Y. C. Jeung and T. D. Chung, *Chem. Eng. J.*, 2022, **429**, 132383.
21 S. Dresp, T. Ngo Thanh, M. Klingenhof, S. Brückner, P. Hauke and P. Strasser, *Energy Environ. Sci.*, 2020, **13**, 1725–1729.
22 I. R. Amador, R. T. Hannagan, A. Qiang, S. Lee, T. Thu, K. M. K. Yap, A. M. Aleman, D. H. Marin, R. Mendoza, M. B. Stevens, F. Jaramillo and A. C. Nielander, *Energy Environ. Sci.*, 2025, **18**, 10195–10204.
23 S. Kim, S. H. Yang, S. H. Shin, H. J. Cho, J. K. Jang, T. H. Kim, S. G. Oh, T. H. Kim, H. S. Han and J. Y. Lee, *Energy Environ. Sci.*, 2024, **17**, 5399–5409.
24 S. Han, S. Sasmal, M. Shen, Y. Wu, O. T. Vulpin, S. Hou, S. Kim, J. Y. Lee, J. Yoon and S. W. Boettcher, *ACS Energy Lett.*, 2025, **10**, 1633–1641.
25 H. Tang, X. Wang, X. Zhao, Y. Dong, B. Xu and L. Wang, *Desalination*, 2023, **561**, 116660.
26 P. K. Giesbrecht and M. S. Freund, *ACS Electrochem.*, 2025, **1**, 667–677.
27 W. Sheng, Z. Zhuang, M. Gao, J. Zheng, J. G. Chen and Y. Yan, *Nat. Commun.*, 2015, **6**, 6–11.
28 B. P. Charnay, Y. Chen, J. W. Misleh, J. G. Wright, R. G. Agarwal, E. R. Sauvé, W. L. Toh, Y. Surendranath and M. W. Kanan, *Nat. Commun.*, 2025, **16**, 9759.
29 T. Zelovich and M. E. Tuckerman, *Membranes*, 2021, **11**, 355.
30 S. Han, H. S. Park and J. Yoon, *Chem. Eng. J.*, 2023, **477**, 146713.
31 S. Han, J. Woo, J. Shim, S. Heo, S. Kim and J. Y. Lee, *Adv. Funct. Mater.*, 2025, **35**, 2508175.
32 S. Han, J. Park and J. Yoon, *Adv. Funct. Mater.*, 2024, **34**, 2314573.
33 Y. S. Park, J. Y. Jeong, M. J. Jang, C. Y. Kwon, G. H. Kim, J. Jeong, J. hoon Lee, J. Lee and S. M. Choi, *J. Energy Chem.*, 2022, **75**, 127–134.
34 H. Xie, Z. Zhao, T. Liu, Y. Wu, C. Lan, W. Jiang, L. Zhu, Y. Wang, D. Yang and Z. Shao, *Nature*, 2022, **612**, 673–678.
35 H. Shi, T. Wang, J. Liu, W. Chen, S. Li, J. Liang, S. Liu, X. Liu, Z. Cai, C. Wang, D. Su, Y. Huang, L. Elbaz and Q. Li, *Nat. Commun.*, 2023, **14**, 3934.
36 S. Xu, J. Chi, T. Cui, Z. Li, F. Liu and J. Lai, *Nano Energy*, 2024, **126**, 109698.
37 Y. S. Park, J. Lee, M. J. Jang, J. Yang, J. Jeong, J. Park, Y. Kim, M. H. Seo, Z. Chen and S. M. Choi, *J. Mater. Chem. A*, 2021, **9**, 9586–9592.
38 L. Guo, J. Chi, T. Cui, J. Zhu, Y. Xia, H. Guo, J. Lai and L. Wang, *Adv. Energy Mater.*, 2024, **14**, 2400975.
39 S. Han, H. Woo, J. Y. Lee, J. Park, S. H. Joo, W. B. Lee, S. W. Boettcher, J. Yoon and J. Ryu, *ChemRxiv*, DOI:https://doi.org/10.26434/chemrxiv.10002078/v1.
40 T. Nishimoto, T. Shinagawa, T. Naito and K. Takanabe, *J. Catal.*, 2020, **391**, 435–445.
41 T. Shinagawa, M. T. K. Ng and K. Takanabe, *ChemSusChem*, 2017, **10**, 4155–4162.
42 J. C. Fornaciari, L. C. Weng, S. M. Alia, C. Zhan, T. A. Pham, A. T. Bell, T. Ogitsu, N. Danilovic and A. Z. Weber, *Electrochim. Acta*, 2022, **405**, 139810.
43 S. Han, J. H. Ryu, W. B. Lee, J. Ryu and J. Yoon, *Small*, 2024, **20**, 2311052.
44 F. T. Haase, A. Bergmann, T. E. Jones, J. Timoshenko, A. Herzog, H. S. Jeon, C. Rettenmaier and B. R. Cuenya, *Nat. Energy*, 2022, **7**, 765–773.
45 J. E. Huang, F. Li, A. Ozden, A. S. Rasouli, F. P. G. de Arquer, S. Liu, S. Zhang, M. Luo, X. Wang, Y. Lum, Y. Xu, K. Bertens, R. K. Miao, C. T. Dinh, D. Sinton and E. H. Sargent, *Science*, 2021, **372**, 1074–1078.
46 S. S. Veroneau, A. C. Hartnett, J. Ryu, H. Hong, C. Costentin and D. G. Nocera, *J. Am. Chem. Soc.*, 2024, **146**, 28925–28931.
47 H. Saada, B. Fabre, G. Loget and G. Benoit, *ACS Energy Lett.*, 2024, **9**, 3351–3368.
48 F. Meharban, X. Tang, S. Yang, X. Wu, C. Lin, L. Tan, W. Hu, D. Zhou, J. Li and X. Li, *Appl. Energy*, 2025, **384**, 125468.
49 L. Yu, M. Ning, Y. Wang, C. Yuan and Z. Ren, *Nat. Rev. Mater.*, 2025, **10**, 857–873.
50 S. Han, J. Kim, J. Shim, W. B. Lee, J. Ryu and J. Yoon, *ACS Catal.*, 2024, **14**, 17525–17534.
51 P. Zhu, Z. Y. Wu, A. Elgazzar, C. Dong, T. U. Wi, F. Y. Chen, Y. Xia, Y. Feng, M. Shakouri, J. Y. (Timothy) Kim, Z. Fang, T. A. Hatton and H. Wang, *Nature*, 2023, **618**, 959–966.
52 M. A. Blommaert, J. A. H. Verdonk, H. C. B. Blommaert, W. A. Smith and D. A. Vermaas, *ACS Appl. Energy Mater.*, 2020, **3**, 5804–5812.

Table of contents (TOC)

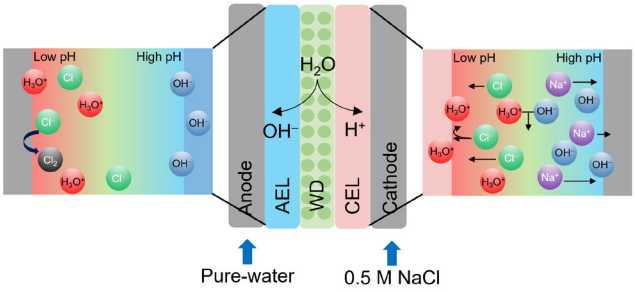

We investigated the local pH gradient that develops at the catalyst–ion exchange membrane interface in a seawater bipolar membrane electrolyzer and mitigated it by minimizing the catalyst–membrane distance. Furthermore, we elucidated the water transport phenomena occurring within the BPM and developed strategies to suppress their adverse effects.